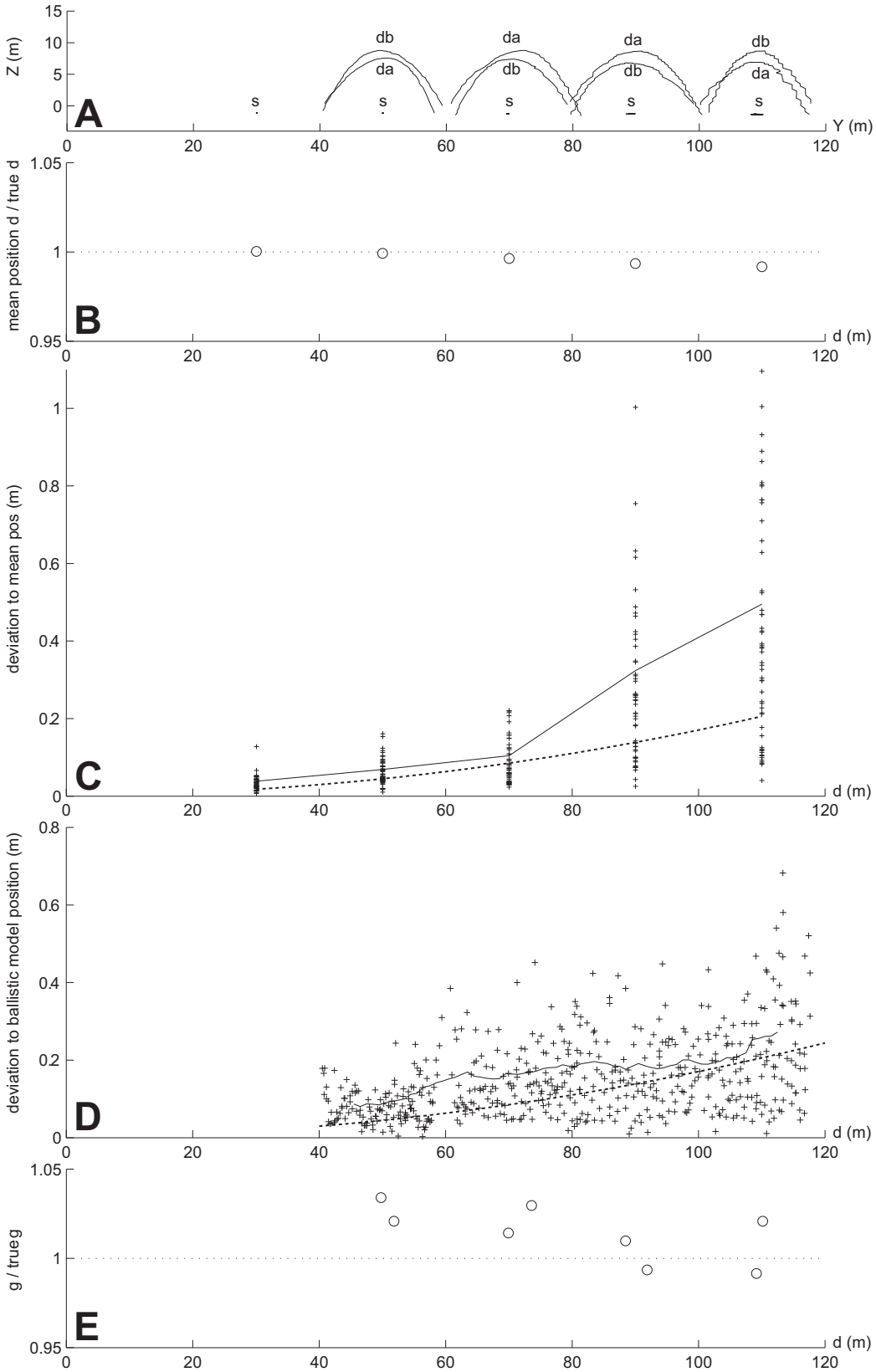

Figure S1: True error estimation procedure, applied to our prototype device (with 323mm eqFL lens) .

Two types of tests are proposed. In the "Static point scanning" test (**SPS**), stationary points (pole with flag) positioned at known distances (30, 50, 70, 90 and 110 m, measured with a band decameter) are filmed while

slowly "scanning" with the apparatus, such that each point is analyzed at various positions (n ≈ 50) throughout the image frame. In the "Dynamic point tracking" test (**DPT**), a tennis ball is tossed at various distances (40 - 120 m), tracked and analyzed at the maximal SF (25 Hz). Reference points for the calibration video were at 20, 40, 60, 80, 100 and 120 m. Tests were performed on a rugby field.

A: side view of test tracks, without any data smoothing. The device is at (0, 0). s: scanned static point; da: dynamic track of ball tossed away from the device; db: ball tossed back towards the device.

B: SPS, systematic error on distance. Plot of the distance to the mean measured position, for each static point, divided by true distance. This first plot can reveal basic distance calibration errors. Here the systematic error was less than ± 1 % of distance.

C: SPS, random error on position. Scatter plot of deviation (m) of each measured position to the mean measured position; solid line: rms value of scatter; dotted line: theoretical value of QPUrms. This plot reveals the amount of random error associated with scanning a point throughout the recorded image. Here the error ranged from .04 m (rms) at 30 m distance, to .50 m (rms) at 110 m. To account for the theoretical effect of distance, the error can be expressed in QPU_{rms} units : here the rms error varied between 1.23 and 2.41 QPU_{rms}, with a higher value at close and far distances, compared to mid-range. Over the whole sampled range (n = 5 points), the mean ratio of random error (rms) to QPU_{rms} was 1.93.

D: DPT, random error on position. Each ball toss track was fitted with a ballistic flight model (see details in fig. S2). Scatter plot of deviation (m) of each measured position to the ballistic model position; solid line: rms value of scatter (10 m-width sliding window, every meter); dotted line: theoretical QPU_{rms}. This plot estimates the amount of random error when tracking a moving, accelerating object. Here the error ranged from 0.09 m (rms) at 45 m to 0.27 m (rms) at 112 m. In QPU_{rms} units, the rms error varied between 1.08 and 2.40 QPU_{rms}, with a higher value at close distances. Over the whole sampled range (n = 68 window steps), the mean ratio of random error (rms) to QPUrms was 1.68.

E: **DPT, error on gravity.** Because the toss starting position and speed are not precisely controllable, properly measuring the systematic error is not possible for DPT. However, the value of gravity (g) returned by the ballistic model (fig. S2) can indicate some error that is not random at the level of one toss (e.g. vertical scaling), and hence absorbed by the model. Here the error was less than ± 3.5 % of true g (9.81 $m.s^{-2}$).

Comments: Both tests are complementary. SPS, performed on well-controlled static points, allows a clear differentiation of systematic and random error components. First, SPS test shows error from space quantization (error source #1, see main text) and image POI placement (#2). In addition, SPS test focuses on calibration errors (#3), which are fully explored by scanning the points throughout the image frame. On the other hand, DPT is less well-controlled (toss initial conditions, wind), relies on a fitting routine to extract random error, and does not provide full access to systematic error. Nevertheless, as DPT implies more strenuous conditions (device angular speed and acceleration), its results more likely reflect the real error during animal flight tracking. In addition to the inevitable error sources #1 and #2, DPT test can reveal in-motion device distortion (#4) and timestamping issues (#5). For a given object movement, these errors will tend to be emphasized at close distance, i.e. when device rotational movement is maximal. On the other hand, as the tracked object is maintained as much as possible in the center of the recorded image, calibration errors (#3) can be less visible during DPT than during SPS test.

About the prototype device used in the present study, we retain that the true random positioning error is approximately doubled compared to the theoretical minimum (QPU_{rms}, eq. 5). As a consequence, with the current prototype, maximal range for field session preparation purposes (table 1) should be considered with a safety margin of about - 30% ($1/\sqrt{2} = .7$, see equation 6). Future technical improvements should focus on mechanical stiffness (DPT results), as well as on calibration procedure (SPS results).

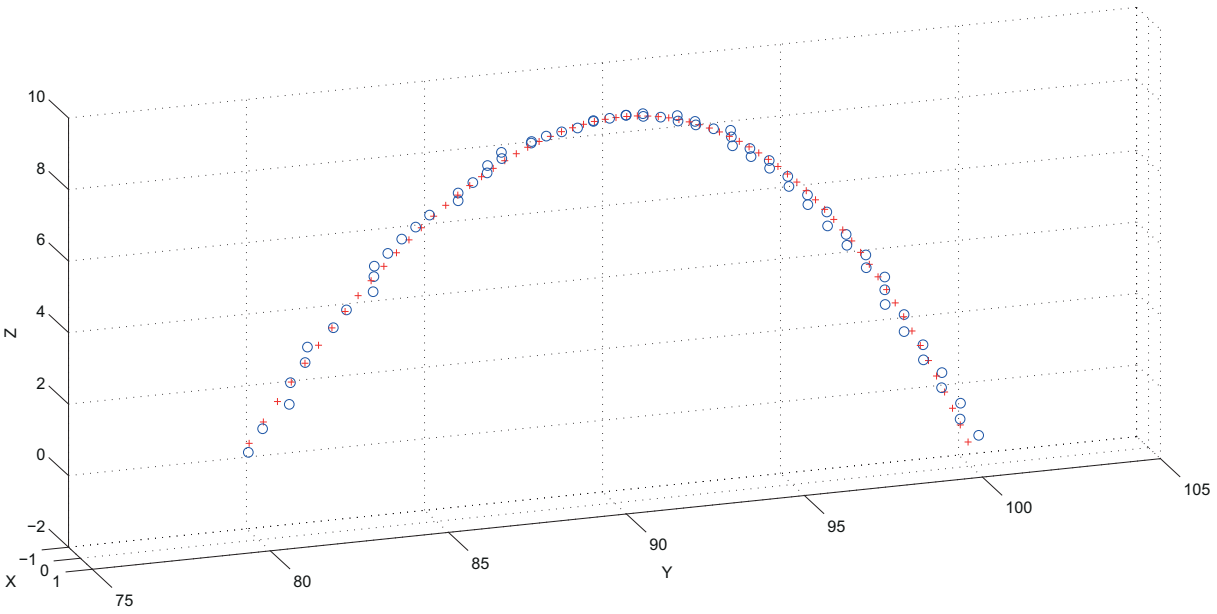

Figure S2: Ballistic flight model.

The numerical mechanical model assumed 2 forces on ball: weight and drag. Drag was proportional to airspeed squared. Airspeed was equal to the composition of ground speed and the opposite of wind speed. The model computed the acceleration, speed and position of the ball every 1/1000 s, and was later down-sampled to 25 Hz. Fixed parameters of the model were tennis ball mass (.057 kg), radius (.033 m) and drag coefficient (.5). Variable parameters were gravity (g), initial position (x_0, y_0, z_0), initial speed (v_0), initial direction (a_0, i_0), wind strength (w) and wind direction (a_w). Wind was assumed horizontal and constant in both time and space. We checked that the returned wind output was compatible with field measurement with a hand anemometer (mean over whole test session: w = 2.1 $m.s^{-1}$, from NW, i.e. aw ≈ - .8 rad). The figure shows an example of model fit output for a ball tossed at 80 m. Circles represent measured positions, crosses represent the model's positions. The fitting routine (Matlab®'s *fminsearch*) returned g = 9.75 $m.s^{-2}$, x_0 = .47 m, y_0 = 79.58 m, z_0 = .88 m, v_0 = 17.3 $m.s^{-1}$, a_0 = 1.68 rad, i_0 = .92 rad, w = 2.15 $m.s^{-1}$, a_w = - .57 rad. The position deviation over the whole flight is .19 m (rms). Note that the effect of space quantization is visible as "stairsteps", especially along the descending (90 – 100 m) part of the track.

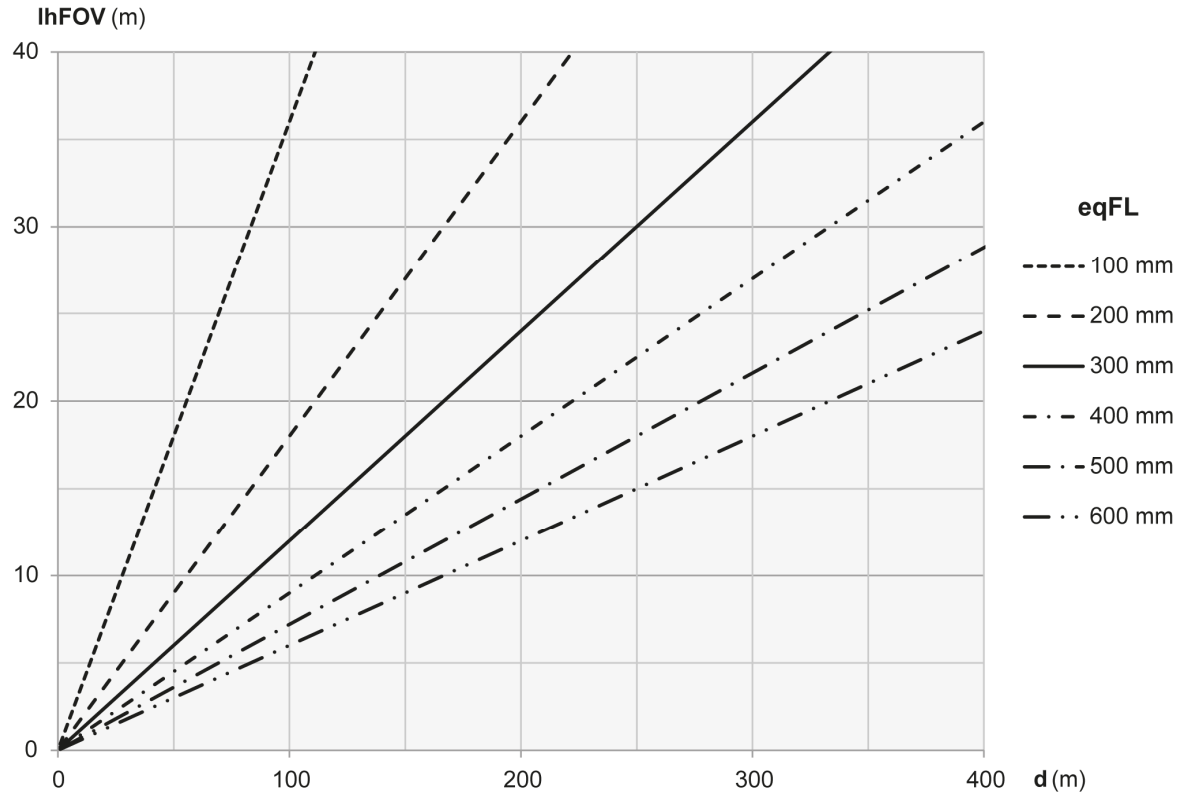

Figure S3: Linear horizontal field of view (lhFOV) as a function of distance (d) and 35mm-equivalent focal length (eqFL)

The plots follow equation A8, for dual cameras. For a single camera with mirrors configuration, the real lhFOV is half the read value. Depending on the size and speed of the animal, small lhFOV values can imply difficulties in keeping the animal in the frame, while large lhFOV values imply a smaller animal image with less behavioural information, but the opportunity to track several nearby animals.

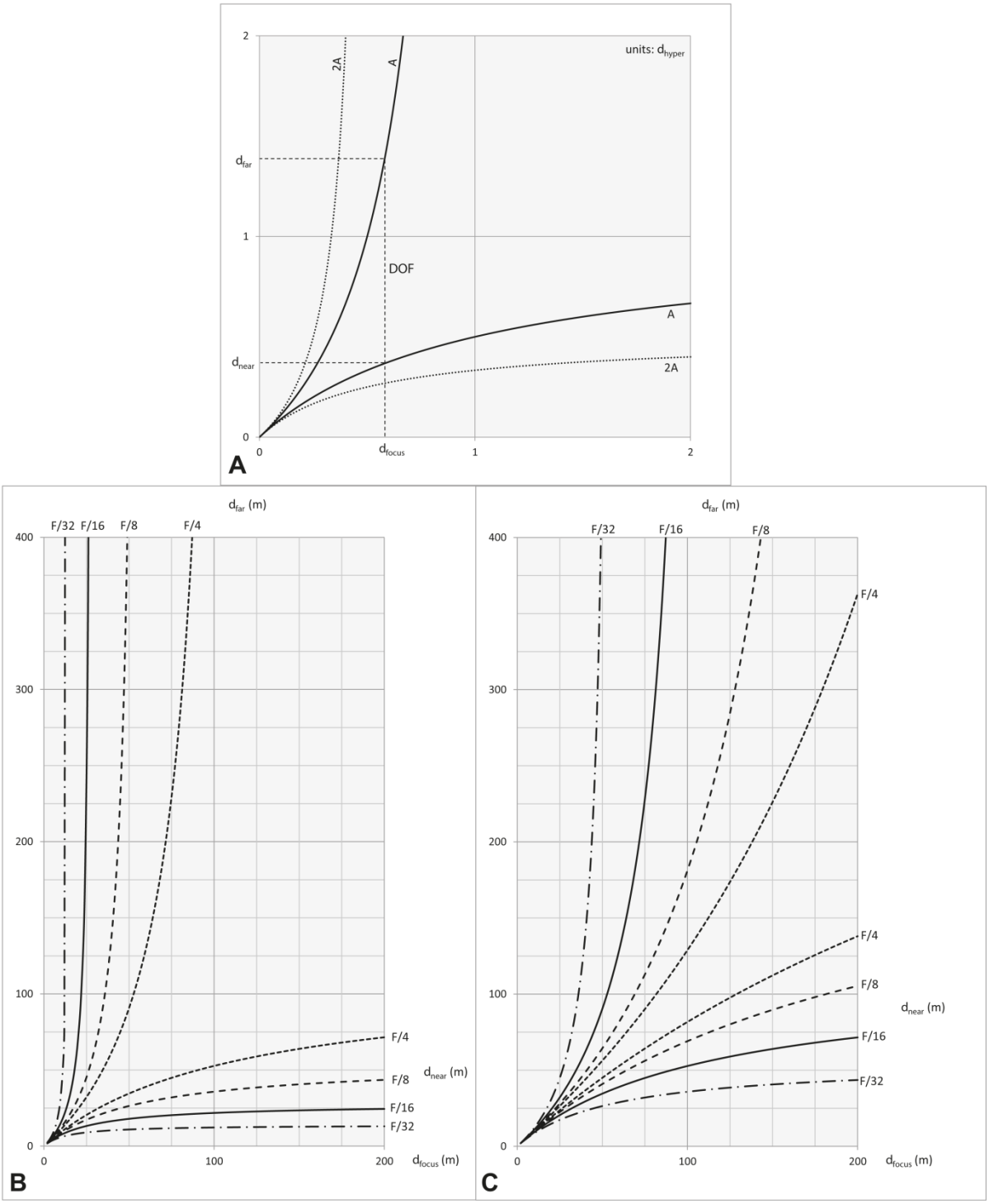

Figure S4: Depth of field (DOF) as a function of focussing distance (d_{focus})

A: Theoretical DOF calculation. For a given focal length (FL), aperture number (A), and circle of confusion (COC), one computes the hyperfocal distance (d_{hyper}), which is the smallest focus distance at which DOF extends to infinity. At shorter focus distances, DOF extends between a near distance of sharpness (d_{near}) to a far distance of sharpness (d_{far}). Closing the aperture (e.g. from f/A to f/2A) increases DOF. We use the classical photographic formulae :

$$d_{hyper} \cong \frac{FL^2}{A\ COC} \quad (S4.1)$$

$$d_{near} \cong \frac{d_{hyper}\ d_{focus}}{d_{hyper} + d_{focus}} \quad (S4.2)$$

$$d_{far} \cong \frac{d_{hyper}\ d_{focus}}{d_{hyper} - d_{focus}} \quad (S4.3)$$

B, C: DOF plots for the camera and lenses we used (B: FL = 200mm ; C: FL = 400 mm). Calculated DOF heavily depends on the chosen COC value (eq. S1), which expresses the acceptable sharpness. A value equal to 1/1250 of the sensor width (SW) is often recommended for photographic work (i.e. .018 mm for our sensor), but tests showed that a value as high as SW/250 was satisfactory for HD video output and our subsequent image analysis. Thus we used COC = .09 mm for these plots.

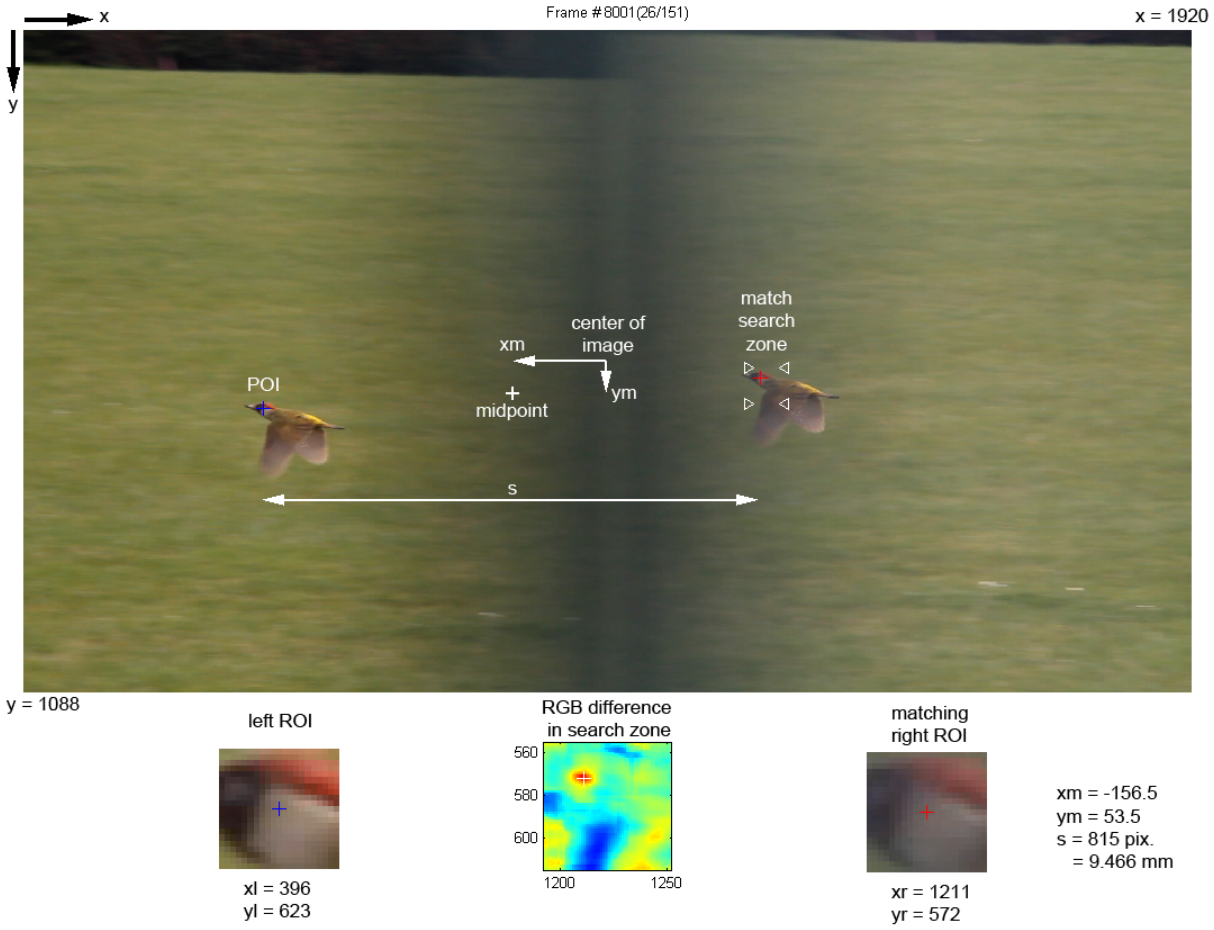

Figure S5: Video frame analysis in Matlab®

Manual operations include (i) positionning a point of interest (POI) on the animal head in the left image and (ii) defining a search zone in the right image. An automatic routine compares the left ROI (10 pixels in both direction around the POI) with all candidate right ROIs (only within the search zone in order to accelerate the routine). The right ROI with the smallest RGB difference is the matching ROI, and its center is considered as the right image of POI. The matching routine yields (x_l, y_l) and (x_r, y_r), and then computes variables that will be used for distance assessment and angle measure correction :

$$s = (x_r - x_l)\left(\frac{SW}{IW}\right) \quad (S5.1)$$

$$x_m = \frac{x_r + x_l - 1920}{2} \quad (S5.2)$$

$$y_m = \frac{y_r + y_l - 1088}{2} \quad (S5.3)$$

Notes: The matching routine is made more robust to right/left exposure variations by mapping the RGB levels of the ROI pixels to 0-255 before comparison. The size of the ROI is of importance: ROI should be large enough to include salient contrast between adjacent pixel zones, on the animal or at the limit between the animal and the background, without including a large background area, potentially containing misleading salient features.